npj | clean water

Article

Published in partnership with King Fahd University of Petroleum & Minerals

https://doi.org/10.1038/s41545-026-00577-4

Carboxylated wood membranes for selective capture and recovery of critical and commodity metal cations

Antoni Sánchez-Ferrer[1] ✉, Devika Upadhye[1], Muzamil Jalil Ahmed[1,2] ✉ & Baohu Wu[3]

Bio-based materials for selective metal cation capture are increasingly sought after as economic and sustainable alternatives to conventional polymeric/ceramic membranes. Here, spruce wood membranes were carboxylated via anhydride esterification with succinic anhydride (SA) and maleic anhydride (MA). Said membranes were used in cation-exchange filtration processes to capture/recover lithium (Li^+) and ferric (Fe^{3+}) ions from aqueous solutions. Structural and chemical analyses, e.g., FTIR, SEM-EDX, WAXS, TGA and DVS experiments, confirmed formation of Na-carboxylate exchange sites, following anhydride esterification and Na-charging with $NaHCO_3$, while preserving the aligned wood microchannel architecture. Gravity-driven filtration experiments demonstrated significant differences as a result of these two modification routes. MA-modified membranes achieved near-quantitative Li^+ removal (≈99.9%) with excellent regeneration stability over three cycles, whereas SA-modified membranes showed greater variability and partial performance decline. For Fe^{3+}, MA-modified membranes exhibited significantly higher, stable removal efficiencies (≈72%) than succinic-modified membranes. Equilibrium ion-exchange experiments showed Langmuir-type monolayer adsorption on chemically homogeneous carboxylate sites, with higher affinity for Fe^{3+} ($K = 0.017–0.020$ L·mmol^{-1}) than for Li^+ ($K = 0.0063-0.0078$ L·mmol^{-1}), reflecting the influence of the cation valence and coordination. Overall, MA modification provides a balanced combination of ion-exchange efficiency, structural robustness, and regeneration compatibility, establishing chemically modified wood membranes as promising, sustainable platforms for metal cation capture and recovery in water treatment applications.

Base/commodity metals, such as Cu, Mn, Pb, Fe, as well as critical/strategic metals such as Co and Li, enter water bodies from mining, battery manufacturing, electroplating, and chemical industries, posing risks even at trace concentrations due to their toxicity and long-term environmental persistence[1]. Conventional treatment processes - including precipitation[2], ion exchange[3], reverse osmosis[4], spray drying[5], adsorption[6], and electrochemical methods[7] - are effective but often constrained by high energy consumption, membrane fouling, operational costs, and limited sustainability.

Recent research has focused on developing high-performance adsorbents and membrane systems to overcome these limitations. Nanostructured metal oxides offer high affinity and rapid kinetics for metal uptake[8], while biomaterials such as chitosan-based sorbents provide tunable chemical functionality through amino and hydroxyl groups, enabling chelation and adsorption of multivalent ions[9–11]. Moreover, the recovery/selective capture of such commodity or critical/strategic metals offers an economic incentive towards closed-loop production processes and circular economy. Membrane-based processes, including ultrafiltration, nanofiltration, and reverse osmosis, also demonstrate high removal efficiency[12–14], although these technologies are limited by high operational pressures, fouling, and the use of non-biodegradable synthetic polymers [15].

Wood has emerged as a promising material for filtration processes due to its renewability, biodegradability, low cost, and mechanical stability[16]. The hierarchical porous structure with aligned microchannels provides a natural scaffold that enables directional water transport, extended residence times, and combined filtration through size exclusion and adsorption[17,18].

---

[1]Wood Materials Science, Wood Research Institute of Munich (HFM), Technical University of Munich, Munich, 80797, Germany. [2]School of Life Sciences, Technical University of Munich, Maximus von Imhof Forum 2, Freising, 85354, Germany. [3]Jülich Centre for Neutron Science (JCNS) at Heinz Maier-Leibnitz Zentrum (MLZ), Forschungszentrum Jülich, Garching, 85748, Germany. ✉e-mail: sanchez.ferrer@tum.de; muzamil.jalil@tum.de

Wood-based membranes have been demonstrated to effectively remove particles, colloids, and microorganisms, with their performance influenced by density, porosity, and pit geometry[19]. Boutillier et al. (2014) reported that xylem tissue from Eastern white Pine could filter up to 4 L of water per day, efficiently removing bacteria via pressure-driven filtration[20]. Contemporary literature also highlights wood's capability to remove nanoparticles and organic contaminants through size exclusion and adsorption as a function of the wood orthotropic direction for some softwoods and hardwoods [21].

Chemical modification significantly improves wood's potential for advanced applications for filtration and resource capture/recovery applications. Currently, the use of modified wood-based membranes is most reported for applications such as anion-exchange/filtration[21–23] (using quaternised woods), dye absorption[24] (using carbonised woods). Specifically, the capture/recovery of commodity or strategic metal cations using wood-based membranes remains largely unexplored[25]. He et al. prepared a wood microfilter by delignification with a deep eutectic solvent, followed by functionalisation with citric acid and cysteine. The resulting wood membrane was grafted with carboxyl $-COO^-$ and sulfhydryl -SH groups, where Cu^{2+} and Cd^{2+} ions could bind and be retained[26]. He et al. prepared a modified wood membrane by grafting poly(acrylic acid) prior to delignification and activation with the radical TEMPO-oxidation. The resulting wood membrane demonstrated good adsorption capacity for Cu^{2+}, Pb^{2+}, Cd^{2+} and Ni^{2+}[27]. Introducing carboxylate-rich functionality into cellulose-based substrates has enabled strong interactions with metal ions in water remediation contexts, motivating ion-binding site engineering in porous cellulose/wood scaffolds[28,29]. A core focus for such materials is based on maintaining stable performance over multiple regeneration cycles.

Particularly for commodity or critical metal cations, e.g., Li^+ and Fe^{3+}, there are few reports of their recovery/capture using a wood-based membrane. Efficient recovery/capture strategies for these commodity/critical metals are necessary to mitigate environmental impacts and facilitate closing production loops or realising a circular economy[30]. Further, the significance of such a proof-of-concept comes at a time when the demand for such resources surges as well as the current industrial shift towards resource recovery from industrial effluents, *e.g.*, battery manufacturing, brine extraction, mining, and electrochemical processes [31].

Bio-based cation-binding membranes and filters reported for metal recovery typically rely on: i) polysaccharide matrices bearing fixed anionic groups, *e.g.*, $-COO^-/-PO_4^{3-}/-SO_4^{2-}$, or ii) biopolymer composites embedded with inorganic selective phases to enhance Li^+ selectivity, *e.g.*, manganese oxide "ion-sieves". Fatima et al. (2026) reported bacterial cellulose acetate membranes embedded with a Li-selective filler hydrogen manganese oxide (HMO), and a piperidinium ionic liquid. The authors reported Li^+ fluxes on the order of 0.1 $mol \cdot m^{-2} \cdot h^{-1}$ with Li^+/transition-metal separation factors of 10–12 using battery-leachate analogues[32]. Recepoğlu et al. (2022) reported cellulosic ion-sorbents and composites, *e.g.*, $-PO_4^{3-}$ or $-SO_4^{2-}$ cellulose derivatives, exhibiting Li^+ uptake capacities in the ~10–35 $mg \cdot g^{-1}$ range and multicycle regeneration in seawater/brine-like matrices[33]. However, across these bio-based platforms, direct comparisons are complicated by differing operating modes - adsorption/diffusion/filtration -, feed chemistries, and regeneration protocols. Importantly, there remains limited literature on multicycle, gravity-driven cation-exchange filtration using an intact wood membrane scaffold in which the cation-exchange sites are introduced by a simple, covalent carboxylation strategy.

Thus, we propose herein two anhydride-based esterification/carboxylation routes, without any delignification or special treatment for the wood scaffold. Esterification with maleic anhydride (MA) or succinic anhydride (SA) introduces $-COO^-$ groups via -COOR linkages that enhance surface charge density, ligand-cation selectivity, sorption capacity and/or metal-binding affinity. Moreover, the cation-exchanging capacity of anhydride-modified wood membranes is investigated, considering the two different cyclic anhydride modifications, *i.e.*, MA vs SA. For the former, the presence of a double bond and the consequent effects on the ligand/group affinity to cations - due to varying acidity - is studied. Finally, most commercial and many reported ion exchange membranes rely on Donnan partitioning and electrically-driven transport for ion-selective separation[34,35]. Here, we target a different operating regime, *i.e.*, a gravity-driven reactive filtration in a porous, renewable scaffold based on wood, where capture is governed by fixed-charge site density and accessibility rather than permselective ion exclusion.

Results and discussion

Wood modification

Spruce wood was chemically modified using two cyclic dicarboxylic anhydrides, i.e., succinic anhydride (SA) and maleic anhydride (MA), to introduce -COOR and $-COO^-$ functionalities onto the lignocellulosic matrix. In both cases, esterification proceeds via nucleophilic attack of -OH groups in the typical anhydroglucose unit (AGU) of the cellulose, hemicelluloses, and lignin. The electrophilic carbonyl groups of the anhydrides' ring undergo a ring-opening reaction to form covalent ester bonds while generating a free $-COO^-$ group[36,37]. Following esterification, soaking of the modified wood in 1 M $NaHCO_3$ replaces the acidic protons of the carboxyl groups with sodium ions, yielding sodium carboxylates that serve as active cation-exchange sites during filtration. Scheme 1 illustrates both anhydride esterification processes, i.e., SA and MA, together with the subsequent Na-exchange (charging) step with 1 M $NaHCO_3$ aqueous solution. The cation-exchanging spruce wood membranes are denoted SSp and MSp, referring to SA or MA esterification, respectively.

For both SA and MA treatments, a 12-fold molar excess of anhydride/AGU was used to promote extensive functionalisation of accessible hydroxyl groups. Based on an earlier work involving lignocellulosic derivatisation, this stoichiometry ensures an excess of reactive groups in the functionalisation and drives high functionalisation density[23,38]. Reactions were carried out in anhydrous *N,N*-dimethylformamide (DMF) under an inert N_2 atmosphere to suppress hydrolysis and oxidative side reactions. The polar, aprotic nature of DMF facilitates swelling of the lignocellulosic matrix and uniform diffusion of the anhydride molecules[39]. This enables efficient esterification while preserving the integrity of the cyclic anhydride until reaction occurs.

In the idealised reaction pathway, up to three anhydride molecules may be grafted onto a single AGU, yielding multi-substituted succinate or maleate derivatives. Both modifications introduce -COOR linkages and $-COO^-$ groups that enhance surface polarity and cation-binding capacity[40]. In case of MA, the presence of an unsaturated $C = C$ double bond alters the electrophilicity of the ester group, contributing to the stronger acidity of the maleic monoester relative to the succinic analogue. A direct comparison of grafting efficiency reveals that SA treatment resulted in a higher degree of modification than the MA treatment. The average weight gain of $w_g = 36.8\%$ for SSp samples (45.1% after Na-exchange) exceeded that of MSp samples of $w_g = 25.1\%$ (30.7% after Na-exchange). This difference reflects the higher reactivity and accessibility of the saturated SA moiety during the esterification process. The post-esterification outcomes are further described in Table 1 below, providing a direct comparison of functional group loading between SSp and MSp.

However, the higher grafting density in SSp samples was accompanied by noticeable changes in physical integrity. SA-modified specimens (SSp) exhibited increased swelling along the radial and tangential directions, as well as bending, warping, and increased brittleness. Similar behaviour in lignocellulosic material modified with SA has been reported elsewhere[36,37,40]. In contrast, MA-modified wood membranes (MSp) retained greater rigidity and dimensional stability. The more moderate and surface-oriented grafting in MSp samples appears to preserve the native wood architecture more effectively, resulting in improved mechanical robustness. These observations indicate a trade-off between grafting density and structural stability[41,42], with important implications for membrane performance under filtration conditions.

Fourier-transform infrared (FTIR) spectroscopy was performed to confirm the chemical modification in Na-charged MSp and SSp wood membranes relative to unmodified spruce (Sp), as presented in Fig. 1,

Scheme 1 | Esterification of spruce wood (AGU) with **a**) succinic anhydride (SA), and **b**) maleic anhydride (MA). A similar mechanism is expected for the free OH groups from hemicelluloses and lignin.

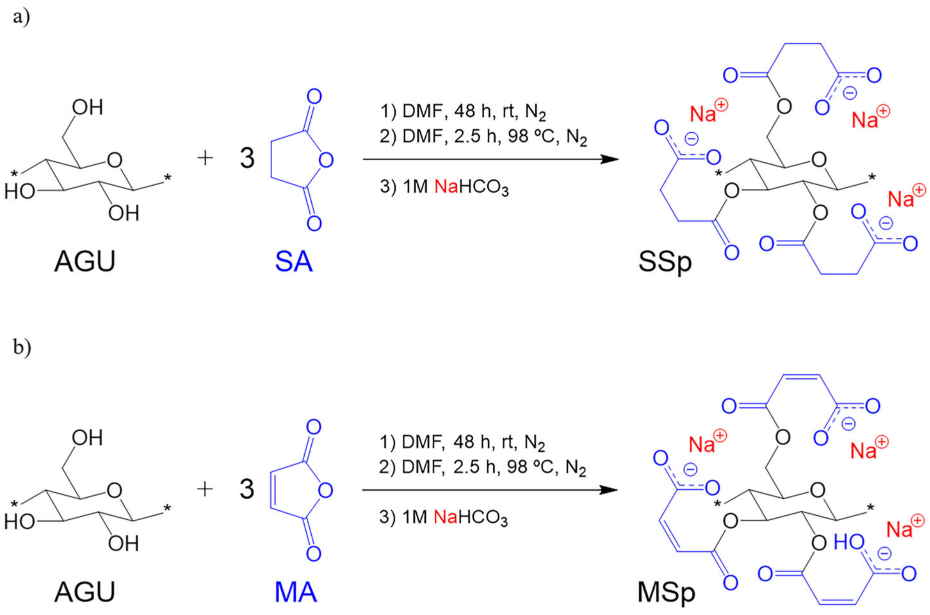

Table 1 | Post-esterification outcomes in terms of theoretical ion-exchange capacity IEC_{max} and weight gain w_g

Sample	Basis	w_g (%)	IEC_{max}[a] (mmol·g⁻¹)
SSp	COOH-based	36.8	2.69
	COONa-based	45.1	2.54
MSp	COOH-based	25.1	2.05
	COONa-based	30.7	1.96

[a] $IEC_{max} = \frac{w_g}{(100+w_g)M_f}$

M_f is the molar mass of the corresponding functional group: SSp-COOH (SA), SSp-COONa, MSp-COOH (MA), and MSp-COONa are 100.07, 122.06, 98.06, 120.04 g·mol^{-1}, respectively.

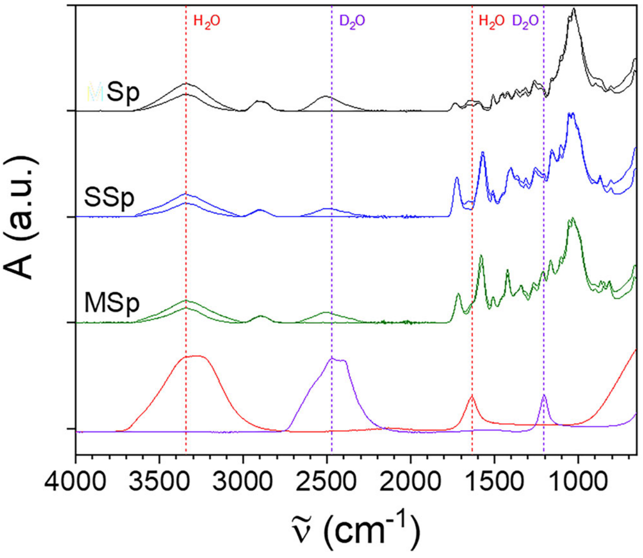

Fig. 1 | FTIR spectra (thick curves) and after D_2O-exchange (thin curves) of unmodified spruce (Sp, black), SA-modified spruce (SSp, blue), and MA-modified spruce (MSp, green) samples. The bottom FTIR spectra correspond to the absorption peaks of free H_2O (red) and free D_2O (violet). All samples were measured after moisture/D_2O uptake and subsequent drying.

together with reference spectra of free H_2O and D_2O. The comparison highlights the distinct chemical contributions in the SSp and MSp spectra after modification. Neat Sp exhibits a broad absorption band between 3300 and 3500 cm^{-1}, corresponding to O–H stretching vibrations in cellulose, hemicelluloses, and lignin. This band is markedly reduced in both SSp and MSp samples, indicating loss of -OH groups through esterification. After exchange with D_2O, the residual O–H bands are attributed to inaccessible -OH groups located within crystalline cellulose regions, with noticeably lower intensities in the modified samples (SSp and MSp). A strong absorption band in the range of 1715–1735 cm^{-1}, attributed to C = O stretching of ester carbonyl groups, appears prominently in both SSp and MSp spectra and is nearly absent in unmodified spruce[40]. The higher absorbance intensity observed for SSp ($A_{1725} = 0.37$) compared to MSp ($A_{1716} = 0.27$) is consistent with the higher grafting degree determined gravimetrically.

Additional bands at 1565–1575 cm^{-1} and 1400–1420 cm^{-1}, corresponding to asymmetric and symmetric stretching of -COO$^-$Na$^+$ groups, confirm successful Na-exchange following $NaHCO_3$ treatment. In MSp, a band near 1630 cm^{-1} is assigned to C = C stretching vibrations, reflecting the presence of unsaturation in the maleic moiety. Overall, the FTIR results unequivocally confirm the successful esterification of spruce wood with both SA and MA and the formation of carboxylate-functionalised membranes suitable for cation-exchange filtration.

Scanning electron microscopy/Energy-dispersive X-ray (SEM/EDX) spectroscopy was performed to evaluate the elemental composition of unmodified (Sp) and chemically modified spruce wood membranes (SSp and MSp). The technique was also used to verify the formation of -COO$^-$Na$^+$ groups following Na-exchange (charging). SEM imaging reveals that the cell wall architecture is well preserved, exhibiting distinct tracheid boundaries and a relatively smooth inner surface. The lumen appears largely unobstructed, and the overall porous softwood matrix is intact. These features align with unaltered lignocellulosic structure, where cellulose microfibrils are embedded in a hemicellulose–lignin matrix without visible surface degradation. This should be the case since any esterification process might only insignificantly increase the molecular distance[42,43]. Both SA and MA modifications introduce surface deposits and slight texturing of lumen edges. These visible changes are consistent with the occurrence of surface chemical modification but do not provide direct information about subsurface or internal cell wall alterations, which cannot be resolved by SEM. Any structural effects are limited to surface coverage by the deposition of reaction products rather than complete obstruction of the lumen architecture.

The EDX spectra recorded in both the longitudinal (L) and tangential (T) directions for untreated spruce (Sp), Na-charged SA-modified spruce (SSp) and MA-modified spruce (MSp) samples are presented in Fig. 2. The Sp EDX spectrum shows only the presence of C ($\kappa_\alpha = 0.277$ keV) and O ($\kappa_\alpha = 0.525$ keV), reflecting the intrinsic lignocellulosic composition of the wood matrix. In contrast, both Na-charged SSp and MSp samples exhibit an additional peak corresponding to Na ($\kappa_\alpha = 1.041$ keV), which is absent in the unmodified wood. The Na signal indicates the successful replacement of H^+ by Na^+ cations following the $NaHCO_3$ treatment and further confirms the presence of accessible -COO^- groups generated through anhydride esterification. The consistent detection of Na in both L- and T-directions indicates that the introduced -COO^- functionalities are not confined to the surface but are distributed within the wood structure accessible to cation exchange.

A semi-quantitative analysis (ad hoc) from the EDX spectra was performed following a series of non-linear fitting approaches. The resulting percentage of COONa domains was 27.6% and 23.2% for the SSp and MSp samples, respectively, which correspond to a mass gain of 38.1% and 30.2% - values close to those from the COONa-based weight gain of 45.1% and 30.7%. Both samples showed the same percentage independently of the L- or T-direction, suggesting a homogeneous distribution of the grafted anhydride along the sample, with deviations from the mass gain values attributed to inhomogeneities, surface roughness, and voids in the samples. These findings corroborate the mass gain and the FTIR results, confirming that the chemically modified membranes possess ion-exchange-active sites, which are essential for subsequent Li^+ and Fe^{3+} filtration experiments.

Scattering experiments (WAXS) were performed to investigate any structural changes in the crystallite domain and the amorphous content in the samples. WAXS analysis is shown in Fig. 3 for the untreated spruce (Sp), Na-charged SA-modified spruce (SSp) and MA-modified spruce (MSp) samples. The described modification does not incur substantial changes to the original structure of the untreated spruce. Therefore, the original monoclinic cellulose I allomorph is retained, having lattice parameters of $a = 0.8$ nm, $b = 0.8$ nm, $c = 1.1$ nm, and $\gamma = 96.9°$. The crystalline peaks (blue curves) allowed for the estimation of the cellulose crystallite's dimensions in terms of average length (l), width (d) and thickness (h) (Table 2), resulting in values relatively consistent after the anhydride modification.

Finally, the degree of crystallinity (χ) was determined from the WAXS patterns, as the ratio between the area of all the deconvoluted crystalline peaks (blue curves) with respect to the total area of the scattering signal (green curve). The results indicate a loss in crystallinity owing to the increasing inclusion of amorphous content in both SSp and MSp samples. This loss in χ corresponds to a change from 66% (Sp) to 40% and 44% for SSp and MSp, respectively, after modification. These values are in agreement with the crystalline content calculated from the weight gain (w_g) for each sample, i.e., 45% and 50% for SSp and MSp, respectively.

Physicochemical properties

Thermogravimetric analysis (TGA) was employed to evaluate the thermal stability and degradation behaviour of unmodified spruce (Sp) and chemically modified spruce wood membranes (SSp and MSp). The normalised mass loss curves (TGA, black) and their corresponding derivative curves (DTG, red) as a function of temperature were recorded under a nitrogen atmosphere and are shown in Fig. 4. All samples were kept at 20 °C and 65% RH prior to the experiment. The analysis of the samples exhibits an initial mass loss below 200 °C associated with the removal of the residual moisture, followed by major thermal degradation stages corresponding to the decomposition of hemicelluloses, cellulose, and lignin [23,37].

Compared to unmodified spruce (Sp), both modified samples (SSp and MSp) show a more pronounced initial mass loss, indicating enhanced water retention due to the introduction of ester and sodium carboxylate functionalities. The dehydration peak temperature (T_w) shifts from 43 °C for Sp to 53 °C for SSp and 47 °C for MSp, reflecting stronger interactions between water molecules and the modified wood matrix. The water content (m_w) approximately doubles for SSp (13.6%) and MSp (11.4%) compared to Sp (6.2%), consistent with the increased number of hydrophilic binding sites introduced by anhydride grafting. The water endset temperature (T_{end}) increases from 137 °C for Sp to 161 °C for SSp and 156 °C for MSp, further indicating stronger water–matrix interactions in the modified membranes.

Beyond dehydration, chemical modification has a significant influence on the thermal degradation behaviour. The onset decomposition temperature (T_{on}) increases slightly for SSp (240 °C) relative to Sp (228 °C), suggesting more extensive bulk modification; however, a decrease is observed for MSp (204 °C), indicating earlier degradation of the esterified regions, probably due to the reactive double bonds present in the maleic motif. The main degradation temperature (T_{max}) decreases markedly from 369 °C for Sp to 316 °C for SSp and 286 °C for MSp, reflecting the lower thermal stability of ester linkages compared to the native cellulose and lignin structures[40,44]. Similarly, the high-temperature degradation peak (T'_{max}), associated primarily with lignin and char decomposition, shifts from approximately 1000 °C in Sp to around 892 °C in both modified samples.

The residual mass at 1000 °C increases substantially upon modification, from 8.6% for Sp to 17.4% for SSp and 13.6% for MSp. This enhanced char yield is attributed to altered pyrolysis pathways and the presence of inorganic sodium species retained within the modified wood matrix[44]. Overall, the magnitude of the thermal shifts correlates with the degree of chemical modification, with SSp exhibiting the strongest water retention, the highest char/ashes residue, and the most pronounced reduction in thermal stability, while MSp displays comparatively milder effects, consistent with its lower grafting density. The quantitative TGA parameters derived from the thermograms are summarised in Table 3.

The reduction in dry thermal stability after anhydride esterification (lower T_{max}) reflects lower thermal robustness of the introduced ester motifs compared with the native lignocellulosic matrix. However, the relevant decomposition temperatures as shown in Table 3, e.g., T_{on} or T_{max}, remain far above conditions encountered in water treatment. In addition, the membranes were routinely dried during preparation at 110 °C without evidence of structural failure, supporting compatibility with moderate thermal handling, e.g., drying, below this range.

Dynamic vapor sorption (DVS) analysis was performed to evaluate the hygroscopic behaviour and moisture responsiveness of unmodified spruce (Sp) and chemically modified spruce wood membranes (SSp and MSp). Moisture sorption and desorption isotherms provide insight into the influence of chemical functionalisation on water uptake, which directly affects membrane transport properties and dimensional stability in aqueous filtration applications. The experimental sorption–desorption isotherms, expressed as moisture content as a function of water activity ($a_w = RH/100$), are presented in Fig. 5.

Unmodified spruce (Sp) exhibited an equilibrium moisture content (EMC) of 22.3% at 95% RH, reflecting the intrinsically hydrophilic nature of native wood arising from abundant hydroxyl groups in cellulose and hemicelluloses domains. In contrast, chemically modified samples (SSp and MSp) showed substantially higher moisture uptake, with EMC values of 56.8% for SSp and 45.0% for MSp. This pronounced increase confirms that esterification and subsequent Na-exchange effectively enhanced the hydrophilicity of the wood matrix through the introduction of ester functionalities and -COO^-Na^+ groups, which exhibit a stronger affinity toward water molecules than the substituted -OH groups.

Notably, SSp samples exhibited the lowest hysteresis between absorption and desorption curves, with a hysteresis factor of $\eta = 1.03$, compared to 1.20 for Sp and 1.17 for MSp. This reduced hysteresis suggests a more homogeneous moisture distribution within the cell wall matrix of SSp, likely resulting from deeper penetration and higher anhydride grafting density. This is also consistent with the higher w_g values. In contrast, the slightly higher hysteresis of MSp may indicate more surface-localised modification, leading to residual polar domains that retain moisture during desorption or hinder water release from the cell wall structure.

All samples exhibited sigmoidal Type II isotherms characteristic of porous biopolymeric materials[43]. The preservation of the isotherm shape in SSp and MSp indicates that the overall pore architecture and capillary

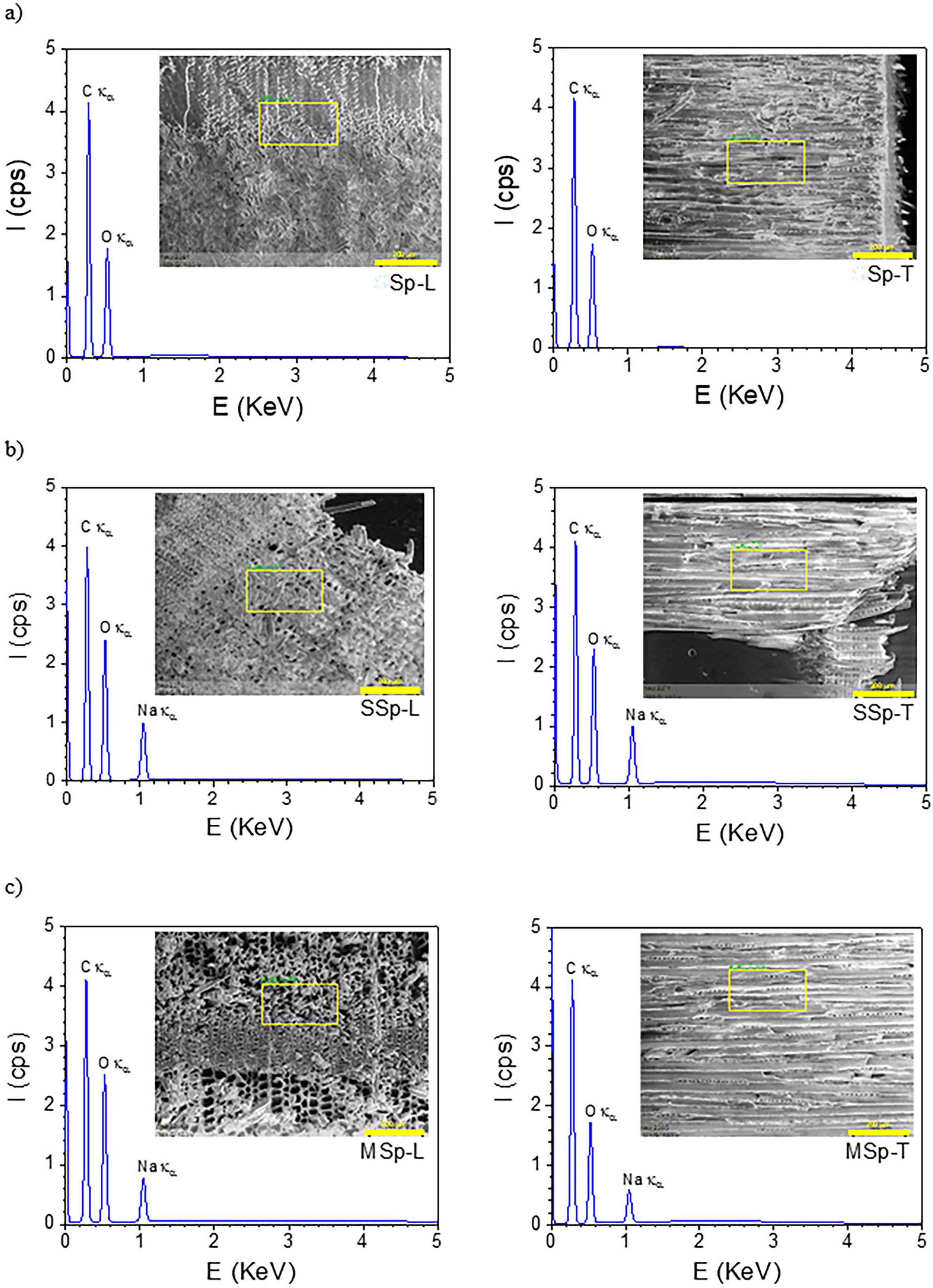

Fig. 2 | SEM and EDX analysis. EDX spectra of spruce wood samples in the L-direction (left) and in the T-direction (right): **a** unmodified spruce (Sp), **b** Na-charged succinic anhydride-modified spruce (SSp), and **c** Na-charged maleic anhydride-modified spruce (MSp) samples. The insets are SEM micrographs, and the scale bars correspond to 200 µm.

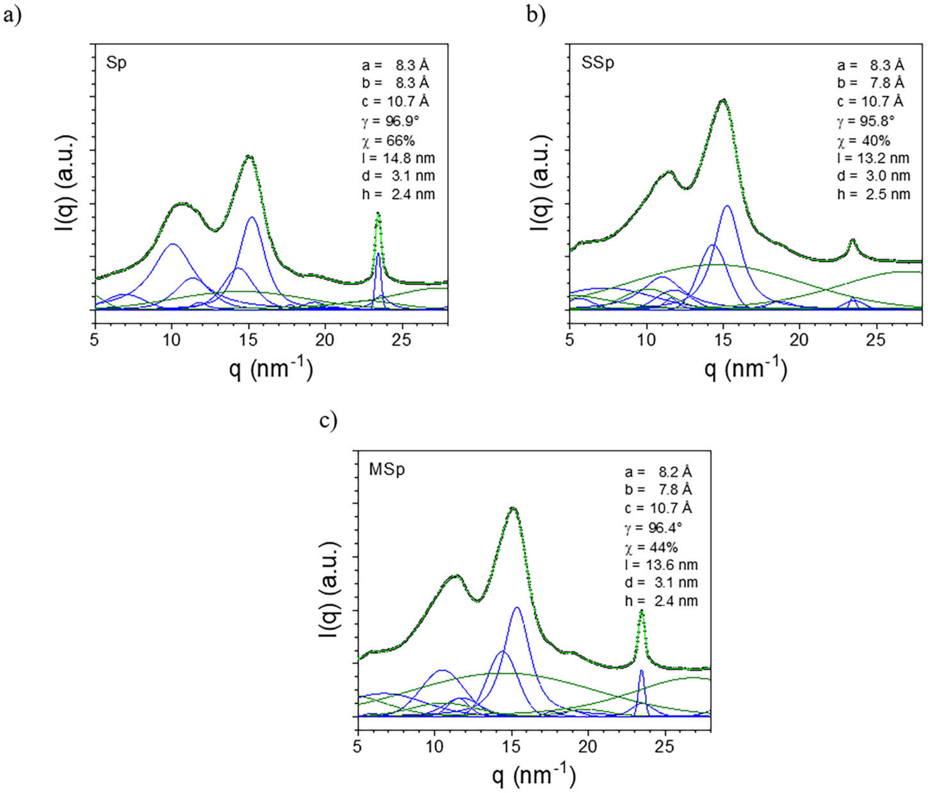

Fig. 3 | WAXS analysis. WAXS profiles for the **a**) untreated spruce (Sp), **b**) Na-charged SA-treated spruce (SSp), and **c**) Na-charged MA-treated spruce (MSp) wood membranes. The light green curves represent the fit to the experimental data by deconvolution into the crystalline (blue) and amorphous (green) peaks.

Table 2 | Lattice parameters (a, b, c and γ), the degree of crystallinity (χ), and the average dimensions of the cellulose single crystal (l, d and h) obtained by WAXS analysis

Sample	a (Å)	b (Å)	c (Å)	γ (deg)	χ (%)	l (nm)	d (nm)	h (nm)
Sp	8.3	8.3	10.7	96.9	66	14.8	3.1	2.4
SSp	8.3	7.8	10.7	95.8	40	13.2	3.0	2.5
MSp	8.2	7.8	10.7	96.5	44	13.6	3.1	2.4

condensation mechanisms remain largely intact following modification, in agreement with SEM observations. However, the increased amplitude of moisture uptake in modified samples reflects altered water accessibility and binding strength due to the introduced ester and sodium carboxylate groups. Quantitative analysis of the sorption behaviour was performed using the GAB and SSO models, with the fitted parameters summarised in Table 4. The monolayer moisture content (MC_0) increased in the order Sp < MSp < SSp, reaching 0.129 g·g^{-1} (7.14 mmol g^{-1}) for SSp and 0.110 g·g^{-1} (6.11 mmol·g^{-1}) for MSp, compared to 0.077 g·g^{-1} (4.28 mmol·g^{-1}) for unmodified spruce. This trend reflects the increasing availability of water-binding sites upon chemical modification, particularly for succinic-treated wood.

Metal cation removal efficiency

Three each of the SA-modified membranes (SSp1–SSp3) and MA-modified membranes (MSp1–MSp3) were tested under identical, dead-end filtration conditions to compare cation-recovery/capture performance. The trials were conducted using aqueous lithium (Li^+) and ferric (Fe^{3+}) solutions using the same membranes. These trials further facilitate the study of site binding effects on a monovalent and on a multivalent metal cation. The anhydride-modified wood membranes were tested across three consecutive cation-exchange/filtration cycles for Li^+ (Fig. SI-1) and for Fe^{3+} (Fig. SI-2). The filtration efficiencies of the membranes were determined using spectrophotometric methods for Li^+ (with alkaline Thorin solution) and Fe^{3+} (with sodium salicylate). Experimental details are given in the Methods section. Table SI-1 and SI-2 show the variations in the Li^+ and Fe^{3+} recovery/capture across the three filtration cycles for the MSp and SSp membranes.

To assess regeneration stability, filtration efficiency was evaluated over three consecutive regeneration/filtration cycles for three independent membranes per chemistry. Regeneration in $NaHCO_3$ is interpreted primarily as ion exchange: Na^+ replenishes the counterions of fixed carboxylate sites ($–COO^-Na^+$), displacing retained Li^+/Fe^{3+} into the regenerant. The pH of such regenerants is mildly alkaline, i.e., pH ≈ 8.3 at 0.1 M $NaHCO_3$, supporting deprotonation of carboxyl groups while avoiding strongly alkaline conditions that would be expected to accelerate ester hydrolysis. This is evident from the fact that the cycle-wise efficiencies η_2/η_1 and η_3/η_1 do not substantially vary (Table SI-3), and remain close to unitary values, *i.e.*, no decay in efficiencies is observed. Cycle-wise efficiencies >100% indicate improved efficiency relative to cycle 1, which is consistent with membrane conditioning and/or more complete Na-form site restoration after the first regeneration.

Generally, for the Li^+ filtrations, the MSp membranes exhibited consistently high Li^+ retention (*ca.* 99.9%), while SSp membranes were relatively variable (*ca.* 90%). For the Fe^{3+} filtrations, MSp membranes exhibited substantial recovery/capture (≈72%) and more uniform Fe^{3+} retention than SSp membranes, which also performed poorly. MSp membranes were more capable of effectively regenerating and sustaining accessibility of their binding sites. MSp membranes maintained an appreciable, yet robust and reproducible Fe^{3+} recovery/capture, while SSp membranes demonstrated a poorer performance. These membrane-specific and cycle-dependent trends are presented in Fig. 6a for Li^+ and Fig. 6b for Fe^{3+}. The cation-exchanging/filtration performance of the MSp and SSp membranes is strongly governed by the nature, spatial distribution, and stability of the functional groups introduced during esterification, whereas unmodified spruce (Sp) membranes retain less than 3% of cations used in this study. Both SA and MA form carboxylated wood matrices via ring-opening reactions with the AGUs' -OH groups. However, their distinct molecular structures lead to markedly different cation-retention behaviour.

Across gravity-driven dead-end tests, the modified wood membranes maintained fluxes on the order of 10^2 L·m^{-2}·h^{-1} (Table SI-4), demonstrating

Fig. 4 | TGA Analysis. Thermogravimetric (TGA, black) and the corresponding derivative (DTG, red) curves for the **a**) untreated spruce (Sp), **b**) Na-charged SA-treated spruce (SSp), and **c**) Na-charged MA-treated spruce (MSp) wood membranes under nitrogen atmosphere from 25 to 1000 °C.

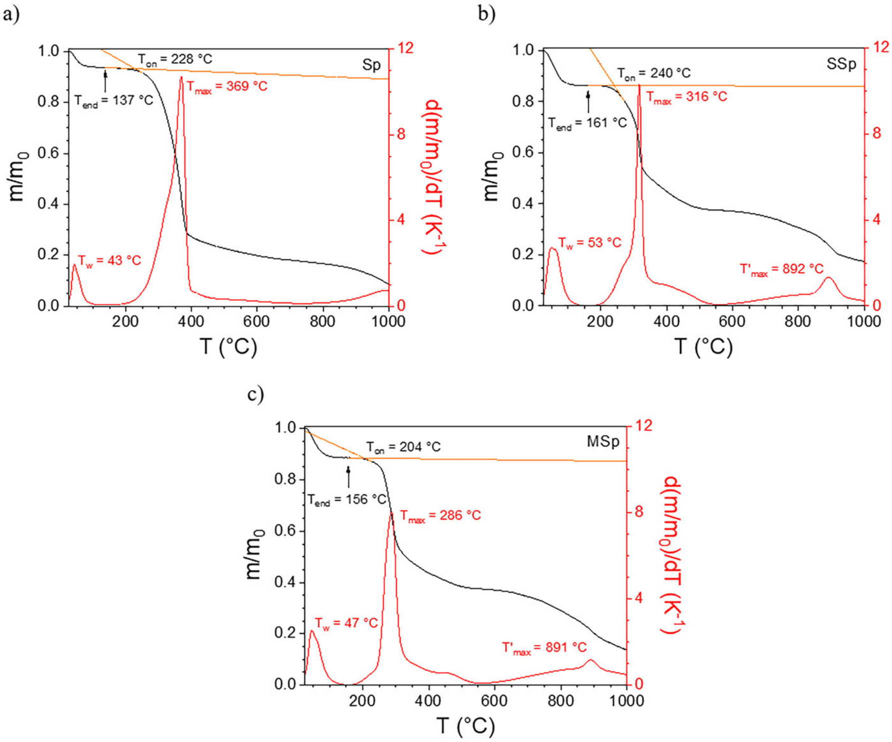

Table 3 | Water peak (T_w), water loss percentage (m_w), and water endset temperature (T_{end}), onset decomposition temperature (T_{on}), maximum decomposition temperature (T_{max}), local decomposition temperatures (T'_{max}), and residual mass at 1000 °C $(m/m_0)_{end}$. Obtained from the TGA analysis

Sample	T_w (°C)	m_w (%)	T_{end} (°C)	T_{on} (°C)	T_{max} (°C)	T'_{max} (°C)	$(m/m_0)_{end}$ (%)
Sp	43	6.2	137	228	369	1000	8.6
SSp	53	13.6	161	240	316	892	17.4
MSp	47	11.4	156	204	286	891	13.6

practical throughput without external force. MSp showed higher average flux than SSp during Li^+ filtration, while Fe^{3+} filtration exhibited lower flux for MSp than SSp, consistent with ion-specific interactions and the different hydration/charge environments of the grafted chemistries. Variability in the fluxes is likely attributed to conditioning effects, channel-to-channel heterogeneity, and ion-specific interactions, i.e., Fe^{3+} complexation. Comparing filtration fluxes with removal efficiencies, Figure SI-3, higher capture efficiencies are achieved without a systematic flux penalty. Within three cycles the dominant performance difference between MSp and SSp is selectivity/affinity of the $-COO^-Na^+$ sites, not permeability constraints.

Ion exchange isotherms

At-equilibrium ion exchange capacity (IEC) experiments were conducted for both Li^+ and Fe^{3+} at varying concentrations using the anhydride-esterified membranes MSp and SSp. These experiments were designed to investigate the intrinsic affinity and saturation behaviour of the $-COO^-$ functionalities introduced via anhydride esterification, independent of flow-induced effects. The experimental data were analysed using Langmuir and the Freundlich adsorption isotherm models, similar to the procedure described in an earlier work [23].

The normalised cation uptake, expressed as the ratio of retained moles (Δn) to the theoretical maximum ion exchange capacity (Δn_{max}), is plotted as a function of equilibrium Li^+ and Fe^{3+} concentration in Fig. 6c, d, respectively. Both models provided comparable fits to the experimental data, each yielding a coefficient of determination $R^2 = 0.93$ (SSp) and 0.91 (MSp) and $R^2 = 0.96$ (SSp) and 0.92 (MSp) for Li^+ and Fe^{3+}, respectively. The fitted Li^+ Langmuir constant for SSp and MSp membranes were $K = 0.0063$ and 0.0078 L·mmol^{-1}, respectively, indicating a moderate but consistent binding affinity of Li^+ toward the carboxylate sites introduced by anhydride modification. For the Fe^{3+} isotherm, the Fe^{3+} Langmuir constant for SSp and MSp membranes was $K = 0.017$ and 0.020 L·mmol^{-1}, respectively. Surprisingly, the ion exchange constant for Fe^{3+} is 2.6–2.7 times higher - stronger affinity - than that of Li^+, showing a correlation with the valence ratio or number of carboxylare motifs required for a trivalent and a monovalent cation.

When analysing the data following the Freundlich adsorption isotherm model, a heterogeneity exponent of $a = 1.0$ was found, effectively reducing the model to a linear form and with the same values as those obtained from the Langmuir adsorption isotherm model. This outcome implies a uniform distribution of binding energies across the membrane surface and supports the assumption of chemically homogeneous carboxylate functionalities formed during esterification. The equivalence of the Langmuir and the Freundlich fits further confirms that cation uptake under equilibrium conditions follows a monolayer, site-saturable exchange mechanism. The stronger Fe^{3+} binding can be attributed to its higher valence and charge density, which enhance electrostatic attraction to negatively charged carboxylate groups. In addition, Fe^{3+} is capable of forming multidentate coordination interactions, potentially involving multiple $-COO^-$ groups per ion, further stabilising adsorption and increasing effective site utilisation.

Fig. 5 | DVS analysis. Sorption isotherms of **a** unmodified spruce (Sp), **b** Na-charged SA-treated spruce (SSp), and **c** Na-charged MA-treated spruce (MSp). The red and blue curves are the adsorption and desorption fitting curves, respectively, from the GAB model, and the green curve is the fitting curve from the SSO adsorption model.

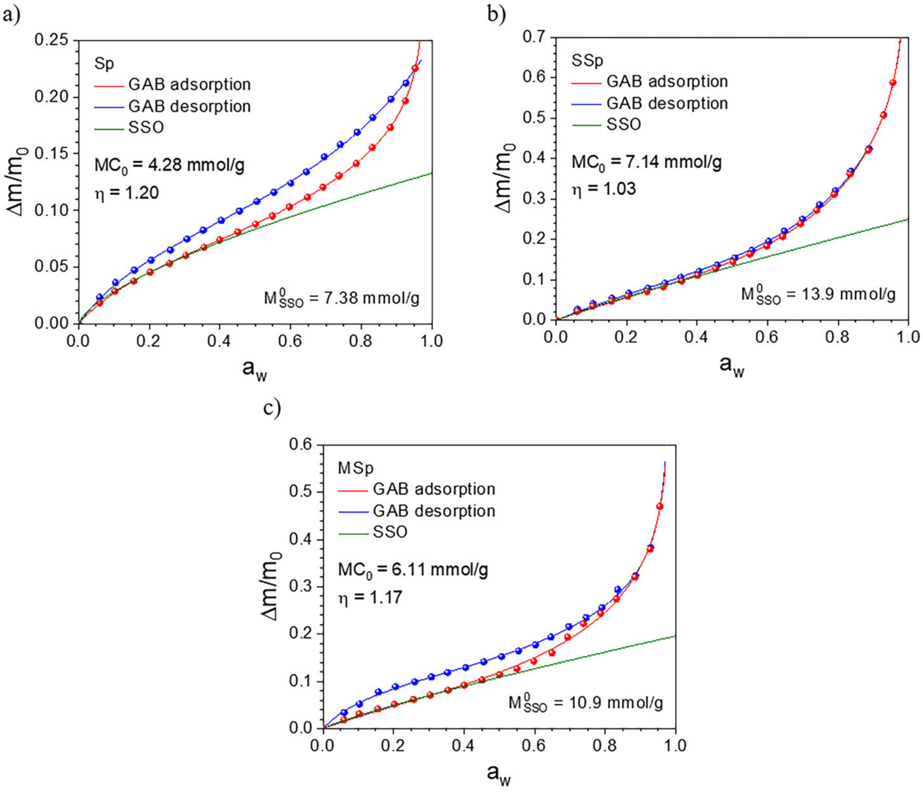

Table 4 | GAB parameters (MC_0, C, K, and N), SSO parameters (M^0_{SSO}, n, and a^*_w), and hysteresis factor (η) obtained from the DVS analysis of the Sp, SSp, and MSp samples

	MC_0	C	K	N	M^0_{SSO}	n	a^*_w	η
Sp	0.077	7.17	0.641	0.0025	0.133	0.67	0.244	1.20
SSp	0.129	2.94	0.817	0.0017	0.250	0.91	0.165	1.03
MSp	0.110	3.21	0.762	0.0053	0.196	0.85	0.187	1.17

Process—property—performance relations

Overall, MA-modification offers a more effective and durable strategy for wood-based cation-exchange membranes, combining high retention efficiency, robust regeneration behaviour, and structural stability. This is attributed to the fact that MA introduces adjacent (vicinal) -COOH groups upon esterification due to the *cis*-configuration of the double bond, resulting in a higher local charge density and enabling multidentate coordination with cations[45]. This structural arrangement is particularly advantageous for Fe^{3+} binding, which requires simultaneous coordination to multiple functional groups. In contrast, SA yields more spatially separated -COOH groups due to the free-rotation of the molecule around the C_2-C_3 single covalent bond. This reduces the likelihood of effective bidentate or multidentate complexation because of the presence of different rotamers[36]. Metal–carboxylate coordination has been analysed computationally elsewhere, showing that complex stability and the maximum number of bound $-COO^-$ depend strongly on metal charge density and carboxylate binding mode. Bidentate binding stabilizes COO-rich complexes and are expected to be particularly relevant for trivalent ions[46]. For monovalent ions including Li^+, DFT studies performed elsewhere indicate preferred coordination by ~3–4 $–COO^-$ oxygen donors in ester-based clusters, consistent with weaker but specific association relative to higher-valence cations[47]. Despite exhibiting higher overall w_g, SA-modified membranes display lower functional efficiency, indicating that extensive grafting does not necessarily translate into improved ion retention. Accordingly, the higher Fe^{3+} affinity and the more stable multicycle performance of MSp can be interpreted as consistent with enhanced multidentate association and reduced sensitivity to partial protonation (lower pK_a value; Fig. 6e), rather than as a uniquely proven molecular binding pathway.

Moreover, due to the presence of the electron-withdrawing double bond in the maleic motif, the pK_a of the free carboxylic acid in MSp membranes is lower (2.62 ± 0.25) than that for SSp membranes (4.42 ± 0.17). This implies that small local changes in the pH medium drastically can alter the binding capacity for SSp membranes, while the binding sites remain almost constant for MSp membranes (Fig. 6e). Therefore, at the pH = 5 and 6.5, the degree of deprotonation for the succinic motifs is *ca.* 79.2% and 97.4%, respectively, whereas for the maleic motifs remains *ca.* 99.6% and 99.96%, respectively. These results underline the importance of functional group proximity and chemical architecture, rather than grafting extent alone in governing ion coordination dynamics and long-term membrane performance in aqueous filtration systems.

The difference between the Li^+ and the Fe^{3+} binding affinity primarily arises from the cation-specific physicochemical properties. Li^+, a small monovalent cation, is strongly hydrated in aqueous solution, and partial desolvation is required for effective interaction with surface carboxylate groups. This energetic penalty limits its binding affinity and reduces site utilisation under equilibrium conditions. In contrast, Fe^{3+} possesses a higher charge-to-radius ratio and stronger polarising power, enabling more effective electrostatic attraction and ligand-like coordination with carboxylate groups, even in partially hydrated states. Moreover, Fe^{3+} uptake reaches higher normalised saturation levels ($\Delta n/\Delta n_{max}$) than Li^+ across the investigated concentration range. This observation suggests that multivalent cations can simultaneously engage multiple functional groups, leading to a more efficient exploitation of available binding sites. In comparison, Li^+ interactions are predominantly monodentate and electrostatic, resulting in lower overall exchange efficiency.

The IEC results corroborate the dynamic filtration findings: while both Li^+ and Fe^{3+} exhibit predictable and model-conforming adsorption on modified wood membranes, Fe^{3+} demonstrates significantly higher affinity

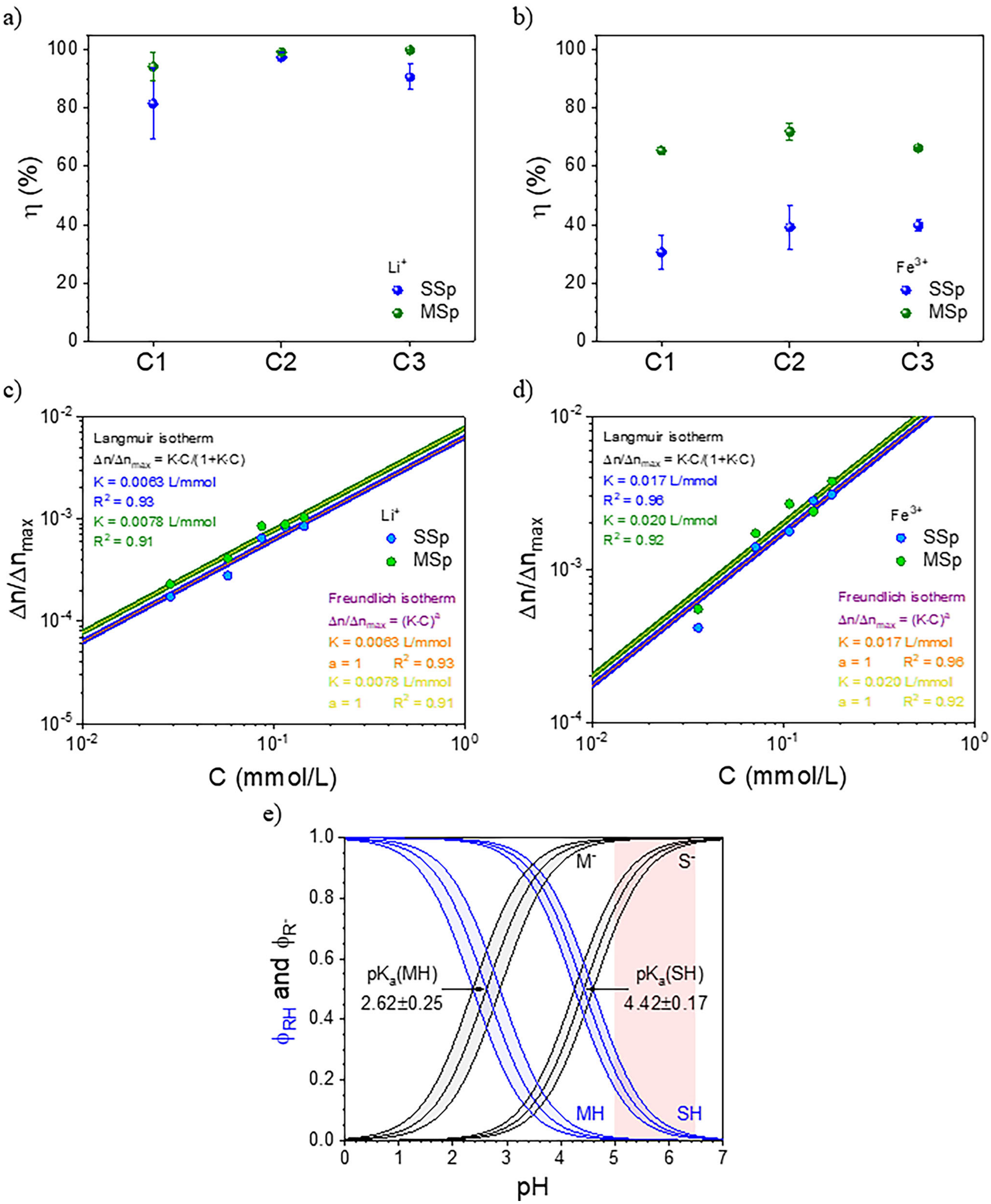

Fig. 6 | Filtration efficiency evaluation, ion exchange isotherms analysis, and pH-dependent membrane protonation/deprotonation. **a** Average Li+ filtration efficiency values for the SSp (blue) and MSp (green) wood membranes for the three consecutive filtration cycles. **b** Average Fe^{3+} filtration efficiency values for the SSp (blue) and MSp (green) wood membranes for the three consecutive filtration cycles. Error bars represent SD/√n across independent membranes ($n = 3$). **c** Li^+ ion exchange isotherms and **d**) Fe^{3+} ion exchange sotherm in terms of change in number of moles (Δn) of available carboxylate sites $-COO^-$ (Δn_{max}) at retention time of 72 h under equilibrium. **e** Molar fraction for the protonated ϕ_{RH} (blue) and deprotonated ϕ_{R^-} (black) species for maleic acid monoester (MH) and succinic acid monoester (SH) in a pH range from 0 to 7. Calculations were done using the Henderson-Hasselbach equation; pK_a values are given in the plot. Individual membrane filtration efficiency values are reported in Table SI-1 and SI-2.

Table 5 | Comparative performance between representative bio-based cation-binding membranes/filters for Li^+ and Fe^{3+}

Membrane/Filter Material	Active Sites	Target cations	Operating Mode	Flux ($L·m^{-2}·h^{-1}$)[a]	pH	IEC_{max} ($mmol·g^{-1}$)	$q_{,max}$[b] ($mg·g^{-1}$)	Regenerability (cycles)	Ref.
MA- and SA-treated wood (MSp/SSp)	$-COO^-$	Li^+ Fe^{3+}	Gravity-driven, dead-end filtration	MSp: 264 ± 125 SSp: 215 ± 63 MSp: 173 ± 69 SSp: 230 ± 69	5–6.5	MSp:2.69 SSp: 2.04	MSp: 14 (Li^+) SSp: 19 (Li^+) MSp: 32 (Fe^{3+}) SSp: 50 (Fe^{3+})	MSp: Stable (3) SSp: Varies (3)	This work
HMO/cellulose	HMO	Li^+	Diffusion cell (no external force)	—	6–7	3.1	21.6	Stable (8)	58
Cross-linked phosphorylated cellulose	PO_4^{3-}	Li^+	Batch, dynamic packed-bed column	390–1559	—	3.6 – 4.9	~25–34	—	33
Sulfonated cellulose microspheres	$–SO_3^-$	Li^+	Batch/column adsorption	5400	4–10	2.35	16	Stable (< 5)	59
Amine-modified chitosan resins	DETA and TEPA polyamines	Fe^{3+}	Column adsorption	764	2.5	DETA: 1.4 TEPA: 3.2	DETA: 78 TEPA: 179	—	60
Chitosan derivatives	ECH, GLA, EGDE	Fe^{3+}	Batch adsorption	—	3	Unmod: 1.67 ECH: 1.29 GLA: 0.92 EGDE: 0.82	Unmod: 91 ECH: 73 GLA: 52 EGDE: 46.	—	9
Nafion™ 117	PFSA (fixed $–SO_3^-$)	Na^+	Electro-chemical/ electro-dialytic processes	—	0-14	0.95–1.01[c]	6 (Li^+) 17 (Fe^{3+})	Stable (high)	61
DOWEX™ 50WX8	Sty–DVB gel resin (fixed $–SO_3^-$)	Na^+	Packed-bed ion exchange	—	0–14	4.24-5.05[d]	30–35 (Li^+) 79–94 (Fe^{3+})	Stable (high)	62

HMO hydrogen manganese oxide, *DETA* diethylenetriamine, *TEPA* triethylenepentamine, *GLA* glutaraldehyde, *ECH* epichlorohydrin, *EGDE* ethylene glycol diglycidyl ether, *PFSA* perfluorosulfonic acid, *Sty–DVB* styrene-divinylbenzene copolymer.

[a] Flux values for packed-bed column studies are not directly comparable to membrane permeance without accounting for bed porosity and pressure drop.

[b] Maximum adsorption capacity, also by definition $IEC_{max} = q_{max} \times |z| / M_{ion}$, where M_{ion} is the ionic weight having equivalent charge 'z'.

[c] Provided by technical supplier as *total acid capacity* (meq/g).

[d] Estimated as: $IEC_{dry}\left(\frac{mmol}{g}\right) = \frac{q_{wet}|z|}{w_{ship}(1-x_w)}$

and capacity. These results highlight the strong suitability of anhydride-modified wood membranes - particularly MA-treated systems or MSp - for removing multivalent metal cations, while also explaining the comparatively moderate yet stable performance observed for Li^+ under both equilibrium and flow conditions. A comparison of the performance of the SA- and MA-treated wood membranes versus other bio-based membranes is provided in Table 5. Note that operating modes and feed chemistries differ substantially across studies, *e.g.*, diffusion/selective transport vs adsorption vs filtration. Table 5 is intended as a contextual benchmark rather than a strictly controlled performance comparison.

To contextualize the functional group loading of the modified wood membranes and to facilitate comparison with the broader ion-exchange literature, we provide a theoretical capacity benchmark in the Supplementary Information (Table SI-5). As apparent with most sustainable, semi-natural substitutes for fossil fuel-derived materials, there is an inherent trade-off between performance versus inexpensively and environmentally friendly material design. While such synthetic membranes demonstrate high separation performance, the MA- and SA-treated wood membranes developed in this study represent a renewable, bio-based alternative, in which ion removal is facilitated by the introduction of -COOH groups.

As described earlier, fewer studies leverage intact wood as a mechanically robust, intrinsically porous scaffold that can be covalently functionalised to introduce fixed-charge exchange sites while retaining microchannel flow pathways. Although the IEC, adsorption/ion uptake and separation efficiency of wood-derived membranes may be lower than those of highly optimised commercial systems, they offer several advantages, including natural hierarchical porosity, low-cost raw materials, and reduced environmental impact.

This study demonstrates that the esterification of spruce wood with cyclic anhydrides effectively transforms native wood into a functional, bio-based cation-exchange membrane for the removal of aqueous Li^+ and Fe^{3+}. Both succinic anhydride (SA) and maleic anhydride (MA) modifications successfully introduced carboxylate functionalities, increasing hydrophilicity and ion accessibility while preserving the intrinsic porous architecture of wood.

Across chemical, thermal, sorption, and filtration analyses, MA-modified membranes consistently outperformed SA-modified counterparts. MA-treated membranes exhibited superior structural stability, higher regeneration resilience, and more consistent multicycle filtration performance, achieving near-quantitative lithium removal (≈99.9%) and significantly higher ferric ion retention (≈72%). Equilibrium ion exchange experiments confirmed a stronger affinity for Fe^{3+} than Li^+, reflecting the influence of cation valency and coordination chemistry, with Langmuir-type monolayer adsorption on chemically homogeneous carboxylate sites. Importantly, high capture efficiencies were achieved while retaining fluxes in the order of $10^2\,L{\cdot}m^{-2}{\cdot}h^{-1}$, supporting a favorable performance–throughput balance for the MSp chemistry in the tested conditions.

The present capture/recovery experiments were conducted in single-solute Li^+ and Fe^{3+} feeds to isolate the role of introduced carboxylate exchange sites under gravity-driven porous filtration. In real-time water samples, abundant coexisting cations, e.g., Na^+, K^+, Ca^{2+} and Mg^{2+}, could compete for exchange sites and may reduce apparent capture efficiencies, particularly for monovalent Li^+. Moreover, given the microporous, aligned channel architecture of wood, the convection-dependent ion transport under flow is expected to impact access to exchange sites, diffusion and site exchange. Therefore, future work will consider validation that requires mixed-ion interference tests, selectivity study, dynamic breakthrough and time-resolved uptake experiments for kinetic studies.

Overall, MA modification provides a balanced combination of ion-exchange efficiency, permeability stability, and mechanical robustness. These findings establish chemically modified wood membranes as promising, sustainable alternatives to synthetic cation-exchange materials and provide a foundation for future development toward selective metal recovery and nitrogen compounds from agriculture and the pharma industry, and scalable water treatment applications.

Methods

Materials

$60 \times 80 \times 2500\ mm^3$ spruce wood timber (*Picea abies*, Sp) was used as the base material, supplied by Rettenmeier Holzindustrie Wilburgstetten GmbH (Germany). Filter discs (50 mm Ø, thickness 2 mm) were cut perpendicular to the fibre direction (longitudinal). Succinic anhydride (SA), maleic anhydride (MA), and anhydrous *N*,*N*-dimethylformamide (DMF) were purchased from Sigma-Aldrich. Lithium chloride (LiCl), potassium hydroxide (KOH), and the arsenazo-based dye Thorin [1-(o-arsenophenylazo)-2-naphthol-3, 6-disulphonic acid, sodium salt] were obtained from Merck (Germany). Ferric chloride ($FeCl_3$), calcium chloride anhydrous ($CaCl_2$), and sodium salicylate were sourced from VWR Chemicals (Germany), while acetone (>99.5) was purchased from ACROS Organics. All chemicals were of analytical grade and used as received. Deionised water (resistivity ≥ 18.2 MΩ·cm) was used for the preparation of all aqueous solutions.

Wood modification using succinic and maleic anhydride

Spruce wood discs ($n = 8$) were divided into two groups for modification with SA (SSp, $n = 4$) and MA (MSp, $n = 4$). Prior to modification, all samples were dried at 110 °C for 2 h, cooled in a desiccator, and weighed to determine the initial dry mass (m_i). For the esterification process, 20 mL of anhydrous DMF was added to sealed 200 mL glass containers with 14 g of either SA or MA corresponding to a glucose-unit-to-anhydride mass ratio of 1:12, and kept at 60 °C under a N_2 atmosphere. After complete dissolution, one pre-dried wood disc was immersed in each container. The samples were left to react for 48–56 h at room temperature. Afterward, the samples were heated at 90 °C for 2.5 h, cooled, and rinsed under flowing deionised water for 30–40 min to remove the solvent and unreacted anhydride molecules. The membranes were air-dried overnight and subsequently oven-dried at 110 °C for 2 h before recording the final dry mass (m_f). The weight gain resulting from chemical modification was calculated as follows

$$w_g(\%) = \frac{m_f - m_i}{m_i} \times 100\% \qquad (1)$$

Fourier-transform infrared spectroscopy

FTIR spectra were recorded using a Nicolet iS50 (ThermoFisher Scientific, USA) spectrophotometer equipped with an attenuated total reflectance (ATR) accessory (diamond/ZnSe crystal). Spectra were collected in the range of 4000–500 cm^{-1} and measured at a spectral resolution of 4 cm^{-1} and averaged over 64 scans. The FT-IR experiments with D_2O-masking experiments were also performed to pinpoint spectral peaks related to the esterification process, other than those of absorbed water. Briefly, by exposing samples to a saturated D_2O atmosphere for 24 h, followed by drying the samples in an anhydrous $CaCl_2$ desiccator prior to analysis.

Scanning electron microscopy/energy-dispersive x-ray analysis

SEM images were captured using a Carl Zeiss EVO-40 XVP (Carl Zeiss, Germany) electron microscope to examine the microstructure of the unmodified and modified wood samples. EDX analysis was also performed to identify the presence of the different atoms in the sample. Operating conditions for the EDX were in low vacuum (≈0.01 Pa) with an accelerating voltage of 15 kV at 97× magnification.

Wide-angle X-ray scattering analysis

The structural analysis of the samples was conducted by wide-angle X-ray scattering (WAXS) experiments using a Xenocs XUESS 3.0 XL KWS-X (France). The scattering patterns were obtained using a high flux Excillum Metal-Jet D2 + X-ray source (Sweden) featuring a liquid metal anode

(250 W; 70 kV; 3.57 mA) with $\lambda_{GaK\alpha}$ radiation of 0.1314 nm. The X-ray scattered intensity was collected using a Dectris 2D Eiger2R 4 M X-ray detector (Switzerland) of 15.5 cm (width) × 16.3 cm (height) and 75 µm resolution, and with a sample-to-detector distance from 0.1 to 1.70 m. An effective scattering vector range of $0.05\ nm^{-1} < q < 45\ nm^{-1}$ was obtained, where q is the scattering wave vector ($q = 4\pi \sin\theta/\lambda$). The degree of crystallinity (χ) was calculated by the deconvolution of the WAXS signal into crystalline and amorphous peaks in the WAXS patterns, the areas of which give the $\chi = A_{crystalline}/(A_{crystalline} + A_{amorphous})$ [38,48,49].

Thermogravimetric analysis

Thermogravimetric analysis (TGA) experiments were performed using a TGA50/M3 from Mettler Toledo and controlled by a TC15 TA controller from Mettler Toledo. A small amount of *ca.* 10 mg of the samples was placed in standard 70 µL aluminium oxide pans. Samples were heated from 25 to 1000 °C at a heating rate of 10 K min^{-1} heating rate and under a N_2 atmosphere.

Dynamic vapour sorption

Moisture sorption behaviour was measured using a DVS device and the experiments were conducted as described by Sánchez-Ferrer et al.[50], using a gravimetric DVS Advantage ET (Surface Measurement Systems, UK) vapor sorption device. The device comprises a microbalance and an N_2-purged chamber with a 200 $cm^3 \cdot min^{-1}$ (12 $L \cdot h^{-1}$) flow at a selected relative humidity (RH). Samples were initially conditioned at 25 °C and 0% RH until completely dry. Measurement starts with the increase in RH of the N_2 flow in steps of 5% until ~100% RH (adsorption). The RH is cycled back (desorption), reducing in steps of 5% until 0% RH. The criterion for change in RH is related to the slope of the water mass uptake during the sorption process (lower than 0.001%·min^{-1} over 10 min). At this point, the sample is measured for one extra hour before changing the RH for the next measuring step. Each dynamic moisture sorption step was analysed using a double stretched exponential (DSE) model[48], and the extrapolated values were used to construct the corresponding moisture sorption isotherms and fitted using the modified Guggenheim, Anderson, and de Boer (GAB) model[51,52]

$$EMC = \frac{\Delta m}{m_0} = \frac{MC_0 \cdot C \cdot K \cdot a_w}{(1 - K \cdot a_w)(1 - (C-1) \cdot K \cdot a_w)} + \frac{MC_0 \cdot C \cdot K \cdot N \cdot a_w^2}{(1 - K \cdot a_w)(1 - a_w)} \tag{2}$$

xwhere Δm is the water mass uptake, m_0 is the dry mass of the sample at $a_w = 0$, MC_0 is the monolayer moisture content capacity, and C, K and N are the GAB fitting parameters.

The sorption site occupancy (SSO) model was implemented to evaluate the number of binding sites per mass of the sample[53,54]

$$M_{SSO} = M_{SSO}^0 \cdot a_w^n \tag{3}$$

wwhere M_{SSO} is the moisture capacity corresponding to the bound water molecules to the sorption sites as a function of the water activity, $M_{SSO}{}^0$ is the maximum amount of bound water, n is the exponent, and aw is the water activity.

UV–vis spectrophotometric Li^+ analysis

Quantitative determination of lithium ion concentrations in filtrate samples was carried out using UV–Vis spectrophotometry based on the formation of a coloured complex between Li^+ and the metallochromic indicator Thorin under strongly alkaline conditions[55]. Calibration standards were prepared at concentrations of 0.2, 0.4, 0.6, 0.8, and 1.0 ppm by serial dilution of a 1000 ppm Li^+ stock solution via a 1 ppm intermediate. Each 2 mL aliquot of Li standard or filtrate sample was mixed with 0.250 mL 10% KOH to establish a strongly alkaline medium, 0.150 mL 0.2% thorin solution as the chromogenic reagent, and 2 mL acetone to enhance complex solubility and stabilise the coloured species. UV–Vis spectra were recorded in the range of 300–700 nm, with deionised water used for baseline correction and reference. A differential absorbance method was implemented by subtracting the spectrum of the 0 ppm Li^+ blank from each lithium-containing spectrum, showing a maximum absorbance at 478 nm (Figure SI-4). This approach isolates the net spectral contribution of the Li^+-thorin complex and effectively removes constant background absorption originating from thorin, acetone, and alkaline media. The resulting differential absorbance values showed excellent linearity across the full concentration range, ΔA(478 nm) = 0.223 C(ppm), and near-ideal linearity ($R^2 = 0.9994$) (Figure SI-5).

UV–vis spectrophotometric Fe^{3+} analysis

Ferric ion concentrations in filtrate samples were quantified using UV–Vis spectrophotometry based on the formation of a coloured coordination complex between Fe^{3+} and sodium salicylate[56]. Calibration standards were prepared at concentrations of 2, 4, 6, 8, and 10 ppm by serial dilution of a 1000 ppm Fe^{3+} stock solution. For complex formation, each 2 mL aliquot of Fe^{3+} standard or filtrate sample was mixed with 2 mL of 0.25 $g \cdot L^{-1}$ sodium salicylate solution. Under mildly alkaline conditions, sodium salicylate forms a stable reddish-purple Fe^{3+}-salicylate complex that exhibits strong absorbance in the visible region. UV–Vis spectra were recorded over the same spectral range of 300–700 nm, with deionised water serving as the baseline and reference. The Fe^{3+}-salicylate complex displayed a well-defined and concentration-dependent absorbance maximum at 490 nm (Figure SI-6). The peak position remained constant across the Fe^{3+} concentration range, while absorbance intensity increased monotonically, indicating the formation of a single dominant complex species. A linear calibration curve was constructed by plotting absorbance at 490 nm against Fe^{3+} concentration, yielding a regression equation, A(490 nm) = 0.00656 C(ppm), with a high coefficient of determination ($R^2 = 0.996$) (Figure SI-7). Given the spectral stability and absence of significant baseline drift (near-zero intercept), no differential correction was required for Fe^{3+} analysis.

Metal cation removal efficiency

A dead-end filtration assembly (47 mm fritted, 40/35, Glassco, VWR, Germany) was used to test the performance of the modified wood membranes in metal cation removal efficiencies η. The effective membrane area and thickness were 1963.5 mm^2 and 2 mm respectively. The dead-end cation-exchange/filtration experiments were performed *as-is* without the need for an external force under ambient conditions. All filtrates were analysed in triplicate using UV–Vis spectroscopy. The metal cation removal efficiency η was calculated as follows:

$$\eta(\%) = \left(1 - \frac{C_p}{C_f}\right) \times 100\% \tag{4}$$

where C_f and C_p refer to the metal concentration, i.e., Li^+ and Fe^{3+}, for the feed and permeate, respectively, where C_f was 1 ppm (50 mL) and 10 ppm (50 mL) for Li^+ and Fe^{3+}, respectively. The feed volume to membrane volume was 12.7 (50 cm^3/3.9 cm^3). The SSp and MSp membranes (3 each) were tested across three filtration cycles for each target metal cation. After each filtration run, membranes were regenerated by immersion in 1 M $NaHCO_3$ overnight to restore the Na-form carboxylate sites, followed by rinsing with deionised water. The regenerant concentration was chosen to provide a large stoichiometric excess of Na^+ relative to the total moles of captured ions per run. The cycle-wise removal efficiency was also calculated to ascertain performance stability, as η_i/η_1, where *i* represents cycle 2 and 3. The filtration flux for each SSp and MSp membranes were also estimated using $J = \Delta V/(A\Delta t)$.

Ion exchange capacity

Li^+ and Fe^{3+} ion exchange experiments were performed using sodium precharged SSp and MSp membranes. Specimens (10 × 10 mm^2) were immersed in Li^+ solutions with concentrations of 0.2, 0.4, 0.6, 0.8, and 1.0 ppm and allowed to equilibrate for 72 h at room temperature. Similarly, specimens ($10 \times 10\,mm^2$) were immersed in Fe^{3+} solutions with concentrations of 2, 4, 6, 8, and 10 ppm and allowed to equilibrate for 72 h at room temperature. Following equilibration, the specimens were regenerated in 1 M $NaHCO_3$ to exchange retained Li^+ or Fe^{3+} with Na^+ cations. The released Li^+ or Fe^{3+} concentration was quantified using UV-Vis spectrophotometry.

The ion exchange capacity (IEC) was calculated from concentration differences before and after sorption, normalised to the dry mass of the samples.

$$\mathrm{IEC} = \frac{\mathrm{n_f} - \mathrm{n_a}}{\mathrm{w_0}} = \frac{\Delta n}{\mathrm{w_0}} \tag{5}$$

where n_f and n_a correspond to the number of moles of Li^+ or Fe^{3+} in the feed and absorbed, respectively. The number of absorbed moles of metal cations Δn can be calculated as $\Delta n = IEC{\cdot}w_0$, and Δn_{max} corresponds to the total number of binding sites, which is essentially the same as the IEC_{max} theoretical value. IEC_{max} value is estimated from the measured mass gain w_g after anhydride functionalisation using both the acid (–COOH) and sodium carboxylate ($-COO^-Na^+$) mass-basis assumptions, and the corresponding theoretical maximum uptake capacities for Li^+ and Fe^{3+} are calculated as $q_{max} = IEC_{max}{\cdot}M_{ion}/|z|$, where M_{ion} is the molar mass for each ion, and $|z|_{Li} = 2$ and $|z|_{Fe} = 3$.

Ion exchange isothermal analysis

The experimental data were analysed using the Langmuir and the Freundlich adsorption isotherm models. The normalised Li^+ or Fe^{3+} uptake, expressed as the ratio of retained moles (Δn) to the theoretical maximum ion exchange capacity ($IEC_{max} \propto \Delta n_{max}$).

The Langmuir model assumes monolayer adsorption on a homogeneous surface with a finite number of energy-equivalent binding sites, and no interaction between cations[57]

$$\frac{\Delta n}{\Delta n_{\max}} = \frac{KC}{1 + KC} \tag{6}$$

where K is the ion exchange constant at equilibrium, and C is the cation feed concentration.

The Freundlich model describes a condition where there is a coverage fraction of 50% chemisorption[57]

$$\frac{\Delta n}{\Delta n_{\max}} = (KC)^a \tag{7}$$

where a is the Freundlich heterogeneity parameter.

Data Availability

The datasets generated and/or analyzed during the current study are not publicly available due to privacy/ethical restrictions but are available from the corresponding author on reasonable request.

Received: 3 February 2026; Accepted: 31 March 2026;
Published online: 20 April 2026

References

1. Lee, H. Y. et al. A selective fluoroionophore based on BODIPY-functionalized magnetic silica nanoparticles: removal of Pb 2+ from human blood. *Angew. Chem. Int. Ed.* **48**, 1239–1243 (2009).
2. Fu, F., Chen, R. & Xiong, Y. Application of a novel strategy—Coordination polymerization precipitation to the treatment of Cu2+-containing wastewaters. *Sep. Purif. Technol.* **52**, 388–393 (2006).
3. Wang, Z., Feng, Y., Hao, X., Huang, W. & Feng, X. A novel potential-responsive ion exchange film system for heavy metal removal. *J. Mater. Chem. A* **2**, 10263–10272 (2014).
4. Sato, T., Imaizumi, M., Kato, O. & Taniguchi, Y. RO Applications in wastewater reclamation for re-use. *Desalination* **23**, 65–76 (1977).
5. Sampaio, C. et al. Chitosan/mangiferin particles for Cr(VI) reduction and removal. *Int. J. Biol. Macromol.* **78**, 273–279 (2015).
6. Alshahateet, S. F., Jiries, A. G., Al-Trawneh, S. A., Eldouhaibi, A. S. & Al-Mahadeen, M. M. Kinetic, equilibrium and selectivity studies of heavy metal ions (Pb(II), Co(II), Cu(II), Mn(II), and Zn(II)) removal from water using synthesized C-4-methoxyphenylcalix[4] resorcinarene adsorbent. *Desalin. Water Treat.* **57**, 4512–4522 (2016).
7. Akbal, F. & Camcı, S. Copper, chromium and nickel removal from metal plating wastewater by electrocoagulation. *Desalination* **269**, 214–222 (2011).
8. Hua, M. et al. Heavy metal removal from water/wastewater by nanosized metal oxides: a review. *J. Hazard. Mater.* **211**, 317–331 (2012).
9. Wan Ngah, W. S., Teong, L. C. & Hanafiah, M. A. K. M. Adsorption of dyes and heavy metal ions by chitosan composites: a review. *Carbohydr. Polym.* **83**, 1446–1456 (2011).
10. Rinaudo, M. Chitin and chitosan: Properties and applications. *Prog. Polym. Sci.* **31**, 603–632 (2006).
11. Wang, B. et al. Selective heavy metal removal and water purification by microfluidically-generated chitosan microspheres: characteristics, modeling and application. *J. Hazard. Mater.* **364**, 192–205 (2019).
12. Bhattacharyya, D., Jumawan, A. B. Jr & Grieves, R. B. Charged Membrane ultrafiltration of heavy metals from nonferrous metal. *Water Pollut. Control Fed.* **51**, 176–186 (1979).
13. Burakov, A. E. et al. Adsorption of heavy metals on conventional and nanostructured materials for wastewater treatment purposes: a review. *Ecotoxicol. Environ. Saf.* **148**, 702–712 (2018).
14. Abdullah, N., Yusof, N., Lau, W. J., Jaafar, J. & Ismail, A. F. Recent trends of heavy metal removal from water/wastewater by membrane technologies. *J. Ind. Eng. Chem.* **76**, 17–38 (2019).
15. Malik, M. A., Hashim, M. A. & Nabi, F. Ionic liquids in supported liquid membrane technology. *Chem. Eng. J.* **171**, 242–254 (2011).
16. Dulneva, T. Y., Deremeshko, L. A. & Ievleva, O. S. Current State and Prospects of Using Lignocellulose (Wood) membranes for water purification. *J. Water Chem. Technol.* **44**, 488–493 (2022).
17. Berglund, L. A. & Burgert, I. Bioinspired wood nanotechnology for functional materials. *Adv. Mater*. **30**, e1704285 (2018).
18. Goldhahn, C. Wood modification with proteins for the development of novel functional membranes. https://doi.org/10.3929/ethz-b-000419271. (ETH Zurich, 2020).
19. Sens, M. L., Emmendoerfer, M. L. & Muller, L. C. Water filtration through wood with helical cross-flow. *Desalin. Water Treat.* **53**, 15–26 (2015).
20. Boutilier, M. S. H., Lee, J., Chambers, V., Venkatesh, V. & Karnik, R. Water Filtration Using Plant Xylem. *PLoS ONE* **9**, e89934 (2014).
21. Sánchez-Ferrer, A. & Guerrero Parra, J. Exploring wood as a sustainable solution for water filtration: nanoparticle removal, size exclusion and molecular adsorption. *Wood Sci. Technol.* **59**, 42 (2025).
22. Jiao, M. et al. Highly efficient water treatment via a wood-based and reusable filter. *ACS Mater. Lett.* **2**, 430–437 (2020).
23. Ahmed, M. J. & Sánchez-Ferrer, A. Wood-supported cationic polyelectrolyte membranes from a reactive ionic liquid for water detoxification. *Chem. Eng. J.* **505**, 158841 (2025).
24. Liu, Y. et al. Functionalization of wood for the removal of heavy metal ions from waster water: a review. *Forests* **16**, 1684 (2025).
25. Trivunac, K. & Stevanovic, S. Removal of heavy metal ions from water by complexation-assisted ultrafiltration. *Chemosphere* **64**, 486–491 (2006).
26. He, L.-T. et al. 3D wood microfilter for fast and efficient removal of heavy metal ions from water. *Langmuir* **39**, 15319–15327 (2023).

27. He, W. et al. Highly nanostructured and carboxylated wood aerogel-based adsorption membrane reconstructed by grafting of polyacrylic acid for efficient removal of heavy-metal ions. *Chem. Eng. J.* **493**, 152411 (2024).
28. Sharma, P. R., Joshi, R., Sharma, S. K. & Hsiao, B. S. A simple approach to prepare carboxycellulose nanofibers from untreated biomass. *Biomacromolecules* **18**, 2333–2342 (2017).
29. Das, R., Lindström, T., Sharma, P. R., Chi, K. & Hsiao, B. S. Nanocellulose for sustainable water purification. *Chem. Rev.* **122**, 8936–9031 (2022).
30. Perveen, S. et al. A Viable and sustainable flat- membrane plate-and-frame module for spent acid regeneration and metal ion recovery. *Heliyon* **9**, e18344 (2023).
31. Al-Rashdi, B. A. M., Johnson, D. J. & Hilal, N. Removal of heavy metal ions by nanofiltration. *Desalination* **315**, 2–17 (2013).
32. Fatima, A., Saif, H. M., Nascimento, F. X., Pawlowski, S. & Crespo, J. G. Selective lithium recovery using bacterial cellulose acetate membranes: toward green recycling of spent Li-ion batteries. *J. Memb. Sci.* **737**, 124776 (2026).
33. Recepoğlu, Y. K. & Yüksel, A. Cross-linked phosphorylated cellulose as a potential sorbent for lithium extraction from water: dynamic column studies and modeling. *ACS Omega* **7**, 38957–38968 (2022).
34. Tang, C. & Bruening, M. L. Ion separations with membranes. *J. Polym. Sci.* **58**, 2831–2856 (2020).
35. Butylskii, D. Y. et al. Review of recent progress on lithium recovery and recycling from primary and secondary sources with membrane-based technologies. *Desalination* **586**, 117826 (2024).
36. Cavdar, A. D., Mengeloglu, F., Karakus, K. & Dizman Tomak, E. Effect of chemical modification with maleic, propionic, and succinic anhydrides on some properties of wood flour-filled HDPE composites. *BioResources.* **9**, 6490–6503 (2014).
37. Teacă, Bodîrlău, C. A. & Spiridon, R. I. Maleic anhydride treatment of softwood – effect on wood structure and properties. *Cellul. Chem. Technol.* **48**, 863–868 (2014).
38. Ahmed, M. J., Wu, B. & Sánchez-Ferrer, A. Anion exchangers prepared from graft polymerisation of microfibrillated cellulose using the reactive ionic liquid. *J. Bioresour. Bioprod.* **10**, 310–324 (2025).
39. Mantanis, G. I., Young, R. A. & Rowell, R. M. Swelling of Wood. Part II. Swelling in Organic Liquids. *hfsg* **48**, 480–490 (1994).
40. Doczekalska, B., Zakrzewski, R. & Bartkowiak, M. Wood esterification by the maleic acid anhydride. *Wood Res* **52**, 79–86 (2007).
41. Gellerstedt, F., WÅgberg, L. & Gatenholm, P. Swelling behaviour of succinylated fibers. *Cellulose* **7**, 67–86 (2000).
42. He, M. et al. Cell wall bulking by maleic anhydride for wood durability improvement. *Forests* **11**, 367 (2020).
43. Essoua Essoua, G. G., Blanchet, P., Landry, V. & Beauregard, R. Maleic anhydride treated wood: effects of drying time and esterification temperature on properties. *BioResources* **10**, 6830–6860 (2015).
44. Leszczyńska, A. et al. Surface modification of cellulose nanocrystals with succinic anhydride. *Polymers* **11**, 866 (2019).
45. Hundhausen, U., Kloeser, L. & Mai, C. Usability of maleic anhydride as wood modification agent for the production of medium density fibreboards (MDF). *Eur. J. Wood Wood Prod.* **73**, 283–288 (2015).
46. Stevens, M. J. & Rempe, S. L. B. Carboxylate binding prefers two cations to one. *Phys. Chem. Chem. Phys.* **24**, 22198–22205 (2022).
47. Dudev, T. & Lim, C. A DFT/CDM study of metal−carboxylate interactions in metalloproteins: factors governing the maximum number of metal-bound carboxylates. *J. Am. Chem. Soc.* **128**, 1553–1561 (2006).
48. Sánchez-Ferrer, A. & Engelhardt, M. Determination of the water diffusivity dependence with the flow rate using a DVS equipment. *Eur. J. Wood Wood Prod.* **83**, 24 (2025).
49. Ahmed, M. J., Wu, B. & Sánchez-Ferrer, A. Quaternised cellulosic materials prepared from chain-growth polymerisation of a grafted reactive ionic liquid. *Discov. Mater.* **6**, 36 (2026).
50. Sánchez-Ferrer, A., Engelhardt, M. & Richter, K. Anisotropic wood–water interactions determined by gravimetric vapor sorption experiments. *Cellulose* **30**, 3869–3885 (2023).
51. Berthold, J., Rinaudo, M. & Salmeń, L. Association of water to polar groups; estimations by an adsorption model for ligno-cellulosic materials. *Colloids Surf. A Physicochem. Eng. Asp.* **112**, 117–129 (1996).
52. Viollaz, P. E. & Rovedo, C. O. Equilibrium sorption isotherms and thermodynamic properties of starch and gluten. *J. Food Eng.* **40**, 287–292 (1999).
53. Willems, W. A critical review of the multilayer sorption models and comparison with the sorption site occupancy (SSO) model for wood moisture sorption isotherm analysis. *Holzforschung* **69**, 67–75 (2015).
54. Willems, W. The water vapor sorption mechanism and its hysteresis in wood: the water/void mixture postulate. *Wood Sci. Technol.* **48**, 499–518 (2014).
55. Thomason, P. F. Spectrophotometric determination of lithium. *Anal. Chem.* **28**, 1527–1530 (1956).
56. Reid, K. R., Meyerhoff, M. E. & Mitchell-Koch, J. T. Salicylate detection by complexation with Iron(III) and optical absorbance spectroscopy. an undergraduate quantitative analysis experiment. *J. Chem. Educ.* **85**, 1658 (2008).
57. Wang, J. & Guo, X. Adsorption isotherm models: classification, physical meaning, application and solving method. *Chemosphere* **258**, 127279 (2020).
58. Tang, L. et al. Highly efficient, stable, and recyclable hydrogen manganese oxide/cellulose film for the extraction of lithium from seawater. *ACS Appl. Mater. Interfaces* **12**, 9775–9781 (2020).
59. Xu, C. et al. Efficient adsorption performance of lithium ion onto cellulose microspheres with sulfonic acid groups. *Quantum Beam Sci.* **4**, 6 (2020).
60. Khalil, M. M. H., Al-Wakeel, K. Z., Rehim, S. S. A., El & Monem, H. A. El. Efficient removal of ferric ions from aqueous medium by amine modified chitosan resins. *J. Environ. Chem. Eng.* **1**, 566–573 (2013).
61. The Chemours Company FC, Product Bulletin P-12. Nafion N115, N117, N1110 (Ion Exchange Materials Extrusion Cast Membranes) (2016)
62. The Dow Chemical Company vols 117-01509 P-9 :Dowex-50-WX8-50-100-resin (1990)

Acknowledgements

All authors further thank Anja Vieler for her assistance in the SEM characterisation of the samples. No funding was received for this research.

Author contributions

A.S.F. contributed with the conceptualisation, data curation, formal analysis, investigation, methodology, resources, software, supervision, validation, visualisation, writing the original draft, and reviewing and editing. D.U. contributed with the data curation, formal analysis, investigation, visualisation, and writing the original draft. M.J.A. contributed with the conceptualisation, data curation, formal analysis, investigation, visualisation, writing the original draft, and reviewing and editing. B.W. contributed with the data curation, investigation, and reviewing and editing. All authors reviewed and approved the final version of the manuscript.

Funding

Open Access funding enabled and organized by Projekt DEAL.

Competing interests

The authors declare no competing interests.

Additional information

Supplementary information The online version contains supplementary material available at https://doi.org/10.1038/s41545-026-00577-4.

Correspondence and requests for materials should be addressed to Antoni Sánchez-Ferrer or Muzamil Jalil Ahmed.

Reprints and permissions information is available at http://www.nature.com/reprints